The Astronomical Journal, 156:60 (8pp), 2018 August https://doi.org/10.3847/1538-3881/aacce4

Small and Nearby NEOs Observed by NEOWISE During the First Three Years of Survey: Physical Properties

Joseph R. Masiero[1], E. Redwing[1,2], A. K. Mainzer[1], J. M. Bauer[3], R. M. Cutri[4], T. Grav[5], E. Kramer[1], C. R. Nugent[4], S. Sonnett[5], and E. L. Wright[6]
[1] Jet Propulsion Laboratory/California Institute of Technology, 4800 Oak Grove Drive, MS 183-301, Pasadena, CA 91109, USA; Joseph.Masiero@jpl.nasa.gov
[2] The Pennsylvania State University, State College, PA 16801, USA
[3] University of Maryland, College Park, MD 20742, USA
[4] California Institute of Technology, IPAC, 1200 California Boulevard, Pasadena, CA 91125, USA
[5] Planetary Science Institute, Tucson, AZ 85719, USA
[6] University of California, Los Angeles, CA 90095, USA
Received 2018 April 27; revised 2018 May 30; accepted 2018 June 12; published 2018 July 24

Abstract

Automated asteroid detection routines set requirements on the number of detections, signal-to-noise ratio, and the linearity of the expected motion in order to balance completeness, reliability, and time delay after data acquisition when identifying moving object tracklets. However, when the full-frame data from a survey are archived, they can be searched later for asteroids that were below the initial detection thresholds. We have conducted such a search of the first three years of the reactivated Near-Earth Object Wide-field Infrared Survey Explorer data, looking for near-Earth objects discovered by ground-based surveys that have previously unreported thermal infrared data. Using these measurements, we can then perform thermal modeling to measure the diameters and albedos of these objects. We present new physical properties for 116 Near-Earth Objects found in this search.

Key words: minor planets, asteroids: general

1. Introduction

The Near-Earth Object Wide-field Infrared Survey Explorer (NEOWISE) has been surveying the sky at two thermal infrared wavelengths since 2013 December 13 (Mainzer et al. 2014a). As part of regular operations, NEOWISE uses the *WISE* Moving Object Processing System (WMOPS) to identify transient sources and link them into tracklets that consist of five observations or more (Mainzer et al. 2011a; Cutri et al. 2015). This length limit was set to balance the reliability of candidate moving object tracklets with survey completeness, while fulfilling the mission requirement of reporting moving object detections to the Minor Planet Center (MPC) within 10 days of the tracklet midpoint.

There are cases where a near-Earth object (NEO) was bright enough to be detected by NEOWISE, but observed an insufficient number of times to be registered by WMOPS. Frequently these are objects that are passing very close to the Earth near the time of discovery, and thus move through the NEOWISE field of regard very rapidly. In other instances, an object's motion may be changing over the observations beyond the set tolerance of the WMOPS software. Because NEOWISE archives and makes available all single-exposure observations, it is possible to search these images for NEO detections missed by the automated pipeline.

In this work, we present such a search of the first three years of the reactivated NEOWISE survey data for close-pass NEOs, similar to the one carried out for the cryogenic NEOWISE data by Mainzer et al. (2014b). The goal of this search is to increase the number of NEOs with physical characterization, and lengthen the orbital arcs of short-arc NEOs with incidental observations beyond the timescale of archived ground-based observations.

2. Methods

Small NEOs are preferentially discovered when they are close to the Earth, as they are at their brightest and thus are easiest to detect. We searched the NEOWISE images for objects in the MPC's list of NEO orbital elements,[7] focusing on objects with provisional designations indicating that they had been discovered in 2014, 2015, or 2016. Although it is possible that some numbered or multi-opposition NEOs were relatively nearby Earth during those years, the astrometry provided by recovered NEOWISE detections will not significantly improve the orbit, and later automated recovery will be easier for these objects. Thus, we focus this work on objects where the observations may provide the biggest gain. Future work will include a more comprehensive search for all known objects that are at, or just below, the single-exposure detection limits.

We used the Solar System Object search tool provided by the NASA/IPAC Infrared Science Archive (IRSA) in the *WISE* image server[8] to determine the predicted locations for all NEOs with provisional designations assigned from the start of 2014 to the end of 2016 for which detections had not already been reported by NEOWISE. This tool uses the spacecraft position as well as the propagated orbit of the asteroid from JPL Horizons[9] to determine if the object was coincident with any recorded NEOWISE image at the time that image was acquired. Our search included both bands acquired by the NEOWISE survey: 3.4 μm ($W1$) and 4.6 μm ($W2$).

While we generally restricted our search to objects with small positional uncertainties at the time of the NEOWISE observations, a broader search for high signal-to-noise ratio (S/N) detections for objects with larger uncertainties was also

[7] https://www.minorplanetcenter.net
[8] https://irsa.ipac.caltech.edu/applications/wise/
[9] https://ssd.jpl.nasa.gov/horizons.cgi

carried out. For 51 objects, the search of the NEOWISE archive recovered observations that fell in between previously published observations and thus had positional uncertainties smaller than the size of the point-spread function (PSF), approximately 6.5 arcsec. The remaining 71 objects were detected by NEOWISE outside of the published observation arc. Of these, three had other observations obtained or linked subsequent to the submission of our astrometry (including 2016 UH_{101}, which was linked to 2010 PP_{58}, an NEO originally discovered by *WISE* during its cryogenic survey). For 44 of the objects where the NEOWISE detections extended the observational arc, multiple NEOWISE detections were obtained along the track at the same positional offsets, confirming these associations as correct.

The remaining 24 objects were observed only a single time, and thus are the most difficult cases to confirm the association between the detection and the object. Five of the single detections were within a 10 arcsec search radius of the predicted position and had an $S/N_{W2} > 5$, making a positive association of the source with the object highly likely. A wider search revealed 15 single detections within 1 arcmin of the predicted position and with $S/N_{W2} > 10$ and low PSF-fit residuals, making them unlikely to be noise. The majority of these also had $S/N_{W1} > 3$, further strengthening the association due to the fact that NEOs tend to be warm and are brighter in *W*2 than *W*1.

The remaining 4 sources (2015 LM_{21}, 2015 VU_{65}, 2016 TX_{17} and 2016 XA_{18}) are lower-confidence associations, but were included as they were deemed to be highly likely to be point sources based on visual inspection. The observations for both 2015 LM_{21} and 2016 TX_{17} were within 1 arcmin of the predicted position, and had $S/N_{W1} > 3$ and $S/N_{W2} > 5$, leading us to conclude these were likely correct associations. The observation of 2016 XA_{18} was within 1 arcmin of the predicted position and had an $S/N_{W2} > 5$, but only an $S/N_{W1} = 2$. This object was located in the overlap region between survey exposures, and the image from 11 seconds later shows a source at the same position, though it was too close to the image edge to be picked up by the pipeline source extraction. This second image supports our association between the detection and object. Finally, the associated observation with 2015 VU_{65} was nearly 3 arcmin from the predicted position, however the source was detected at $S/N_{W2} = 20$ with a low residual for the fit of the PSF to the detection, making it unlikely to be a cosmic ray.

Following the procedure used in our previous publications (e.g., Mainzer et al. 2014b; Masiero et al. 2017, etc.) we took all the detections of our objects of interest that had been submitted to, accepted by, and published by the MPC, and searched the NEOWISE Reactivation Database L1b source table on IRSA. For each detection we search within 6 arcsec of the reported position, with a further constraint of 5 s on the difference between the reported and observed MJD. This query returned the 3.4 and 4.6 μm profile-fit magnitudes and associated errors for each detection, as well as any coincident sources in the AllWISE Atlas detection database. The AllWISE Atlas is a deep-stack of the *WISE* primary-mission data with the number of coadded images rising from $\sim$8 at the ecliptic to $>$100 closer to the poles(Cutri et al. 2014). This ensures that the detection in the NEOWISE survey data is not of a faint background object with varying brightness. We searched the Atlas at the position of each detection with a radius of 6 arcsec, and rejected any detection that was found with $S/N > 7$ in either band in the Atlas. Because Atlas sources are extracted from stacks of $>$10 single-frame images, this S/N cut will capture high-confidence background objects significantly below our nominal detection limit that may be experiencing a transient brightening event, while minimizing the chances of rejecting a detection due to a much fainter coincident background source.

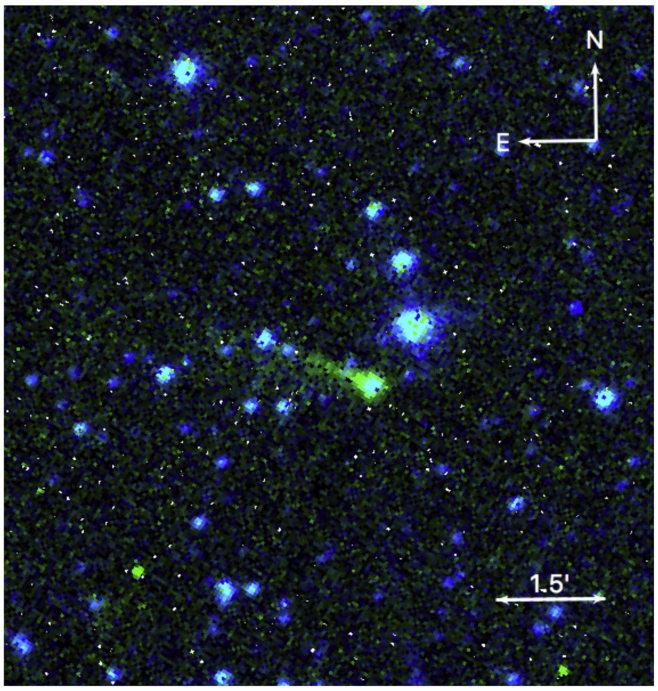

Figure 1. NEOWISE 2-band image of near-Earth object 2014 XK_6 (center) showing clear signs of cometary activity with a tail extending $\sim$1.5 arcmin to the ENE, consistent with the anti-sunward direction. *W*1 (3.4 μm) is shown in blue, and *W*2 (4.6 μm) is shown in green.

NEOWISE simultaneously acquires images at 3.4 μm and 4.6 μm (referred to as *W*1 and *W*2, respectively). For objects detected in both bands, we require that the object has an NEO-like color (i.e., $W1 - W2 > 1$ mag, as opposed to stars that usually have a color of $W1 - W2 \sim 0$). We detect 33 asteroids in a single NEOWISE exposure set and 89 in multiple exposures, for a total of 354 visually confirmed detections of 122 NEOs. The astrometric observations of these objects were reported to the MPC, and the orbital solution that was computed after the inclusion of these observations was used for our thermal fitting to ensure the most accurate distance measurements at the time of observation for these close-pass objects. We use the updated orbital elements, along with the time of observation and reported spacecraft positions to calculate the heliocentric and geocentric distances and phase angle at the time of observation. These parameters are also available via JPL Horizons.

During the course of our search we identified one object, 2014 XK_6, that showed clear signs of cometary activity. This NEO was observed a single time by NEOWISE, and detected in both bands. We present the 2-band NEOWISE image in Figure 1, which clearly shows the cometary activity detected. Astrometry for this object was reported to the MPC, but no other detections of activity have been found by other surveys, including in the Pan-STARRS discovery images obtained one month after the NEOWISE detection (R. Weryk et al. 2017,

private communication). 2014 XK_6 has a Tisserand parameter of $T_J = 2.9$, consistent with a Jupiter-Family Comet. It is possible that this object is similar to NEO (3552) Don Quixote, which also revealed a tail in the infrared that was not seen in optical measurements (Mommert et al. 2014), indicating either weak, sporadic activity, a large contribution from CO_2 emission (which falls in the *W*2 bandpass), or both.

We note that for 19 of our targets, we find 5 or more detections in the *WISE* single exposures. In theory, these nominally should have been detected by WMOPS. In 6 of these cases, the object fell below the single-exposure detection limit of S/N = 4.5 used by WMOPS and thus did not have sufficient data to construct a tracklet. In 6 other cases, the object was observed near the ecliptic or equatorial poles, where assumptions about the linearity of short-term on-sky motion in the rectilinear coordinate system made by WMOPS are not valid. For the remaining seven objects, during close approach to Earth their tracklets deviated from linear motion significantly enough over the time span covered by the NEOWISE observations to not be linked by the WMOPS software. These objects all present compelling evidence for the benefits of archiving all recorded images from surveys to allow for later re-analysis.

3. Thermal Modeling

We use the Near-Earth Asteroid Thermal Model (NEATM, Harris 1998) to determine the physical properties of the observed NEOs, following the process and selection criteria described in our previous work (e.g., Nugent et al. 2015, 2016; Masiero et al. 2017). In brief, we extract NEOWISE *W*1 and *W*2 magnitudes and errors using IRSA with the positions and times reported to the MPC. All of our detections were visually inspected to ensure they were not incorrect associations with cosmic rays, diffraction spikes, nebulosity, or other sources of false detections, and over half of our objects were detected in two bands at S/N > 3. Using the MPC-published *H* and *G* photometric parameters for each object along with the orbit, we determine the expected visible brightness at the time of each observation. As most of our observations tend to be close in time to ground-based detections, this method should in general result in reasonable estimates for the visible brightness even if the *H* and *G* parameters are not well-constrained. However, systematic errors induced by the assumed color corrections known to be present in the published MPC *H* magnitudes will still impact our fits (cf. Vereš et al. 2015; Masiero et al. 2017).

Included in the assumptions we make for our thermal modeling is that the emissivities of the asteroids are uniformly $\epsilon = 0.9$ at all bands. As pointed out by Myhrvold (2018), this may violate Kirchhoff's law if the point reflectance of the surface material is not 0.1. However, as emissivity and beaming parameter jointly modify the characteristic temperature modeled by NEATM, the uncertainty in emissivity (typically of order 10%) is subsumed by the much larger uncertainty on the beaming parameter (of order 50% for NEOs). In fact, some of the variation in beaming parameter is likely due to variations in emissivity, and thus these variations are properly accounted for in our model.

Further, Myhrvold (2018) shows that the vast majority of asteroids and analogs have emissivities within ~10% of 0.9. An important caveat is that Myhrvold (2018) neglected to account for the uncertainty on the *G* phase slope parameter when calculating emissivity from measured albedos; the true range of variations of *G* away from the default assumption of 0.15 (of order 66%, cf. Lagerkvist & Magnusson 1990), when included in the calculation, results in an uncertainty on emissivity that means the determined values are consistent with 0.9 for nearly all cases, further validating our assumptions. As an example of the variation possible in the *G* parameter, we show in Figure 2 all values of *G* listed as fitted in the PDS Asteroid Absolute Magnitude and Slope data set (Tholen 2009). This histogram shows that the default assumed value of $G = 0.15$, while being roughly a median value for the population, falls between the peaks of the weakly bimodal distribution of *G* values. Additionally, fitted *G* parameters cover a large range of values, which would propagate directly to a large uncertainty when calculating emissivity from *G*. The relation between emissivity and geometric albedo (from Bowell et al. 1989) is written:

$$1 - \epsilon = A = qp_V = (0.29 + 0.684G)p_V.$$

The effect of the possible range of values of *G* on the final computed ϵ depends on the albedo of the material, with higher albedo materials showing a more significant effect. However, the uncertainty on *G* cannot be ignored categorically.

Using our *W*1 and *W*2 measurements, inferred *V* magnitude, heliocentric and spacecraft-centric distances, phase angle, and assumed infrared albedo ratio ($\frac{p_{IR}}{p_V} = 1.6 \pm 1.0$) we simultaneously constrain the diameter and V-band albedo for each object using a least-squared minimizer available through the *scipy* Python package[10] (Jones et al. 2001). We set a limit of $\sigma < 0.25$ mag on the uncertainty of the measured magnitude in each band for it to be used in the thermal fitting; detections with larger measurement uncertainties were not used as model constraints. If the *W*1 and *W*2 fluxes are both dominated by thermal emission (i.e., the reflected light component is <10%) we can constrain the beaming parameter. For objects detected in only a single band, or that are dominated by reflected light in *W*1, we assume a beaming parameter (η) of 2.0. The assumed beaming parameter we choose here is larger than what was assumed in other thermal modeling papers of NEOWISE data (e.g., Nugent et al. 2015, 2016; Masiero et al. 2017), and is instead drawn from the mean of the fitted beaming parameters

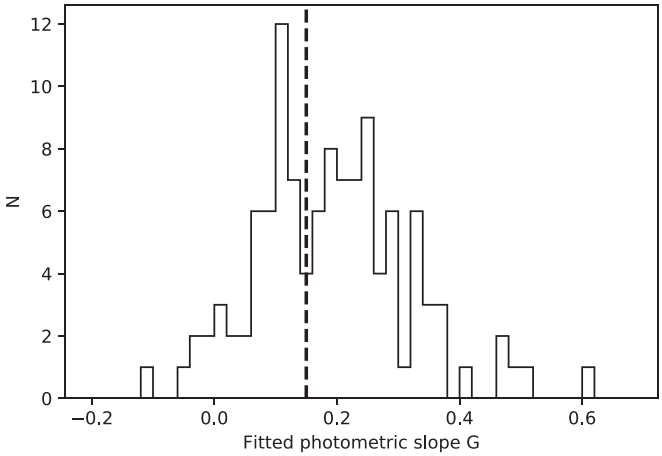

Figure 2. Distribution of all fitted photometric *G* slopes in the Tholen (2009) PDS archive. The default assumed value most commonly used for asteroids, $G = 0.15$, is shown as a vertical dashed line. Fitted values can vary by over 100% from the assumed value.

[10] https://www.scipy.org

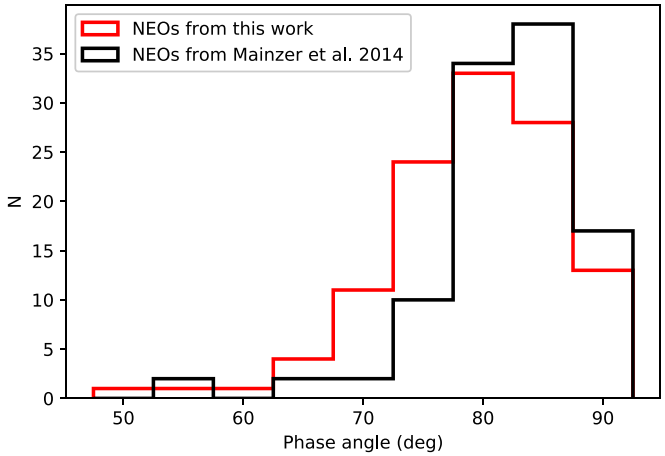

Figure 3. Distribution of observed phase angles for all NEOs presented here (red) and those from Mainzer et al. (2014b) (black).

for small NEOs found in Mainzer et al. (2014b). We show in Figure 3 that the distribution of phase angles for our objects is comparable to those from Mainzer et al. (2014b), and thus the larger assumed beaming parameter is appropriate because these close-pass objects are at higher phases on average and in general smaller than NEOs detected by WMOPS Wolters & Green (2009), Mainzer et al. (2011b).

In order to determine uncertainties on our fitted physical properties, we perform 25 Monte Carlo simulations of each fit, varying the measured magnitudes within their measurement uncertainties, and assuming a random error of 0.2 mag for H, 0.5 for η (when not fit), and 1.0 for the infrared albedo ratio. These parameters match our standard assumptions for NEOs from previous work (cf. Mainzer et al. 2011b, 2014b) and are used to encapsulate the range of values these parameters are observed to have. In addition to the random error determined through Monte Carlo trials, we add an additional diameter uncertainty due to the incomplete rotational phase coverage for objects with a small number of detections (see below).

We reject from our fits any object where the final reflected light component in $W2$ was >10% of the total flux. Thermal fits to $W2$ can be significantly altered by assumptions of the NIR albedo, and lead to unstable solutions. We have found in previous work that a cut at 10% reflected light results in a more reliable list of physical properties (Masiero et al. 2017). Table 1 gives our fitted diameters and albedos for the 116 NEOs.

3.1. Diameter Uncertainty

Thermal modeling using NEATM results in a constraint on the equivalent circular diameter of the projection onto the sky of the true three-dimensional shape of the observed asteroid at the time of observation. If the object has been observed at multiple different rotation phases, the best simultaneous fit of all observations thus corresponds to the spherical-equivalent flux for that viewing geometry. Multiple observing epochs can reduce the uncertainty due to pole-on versus equator-on viewing geometries. However, for objects observed only a few times, or even a single time, the fit would instead constrain a sphere with proportions set by the effective circular area of the object at the time of observation. Thus, the uncertainties on diameter for the fits presented here tend to be larger than for objects with better coverage, even when both bands are thermally dominated and a beaming parameter can be fit. For nearly circular objects this additional error will be small, while for very elongated shapes, it can be the dominant source of error.

The error due to unknown rotation phase is a function of the number of detections, and the amplitude of the light curve. To test the effect of the unknown light curve on the measured flux, we perform a Monte Carlo simulation of N random samples of a theoretical light curve with amplitude A. We compare the average from those N samples to the true mean of the light curve, and characterize the light curve-induced deviation as a fraction of A. As light curve amplitude is measured peak-to-trough, the maximum possible deviation is 50% A, while on average a single observation will result in a mean deviation of 32% A from the midpoint of the light curve. As the number of observations N increases, and the light curve is better sampled, the mean deviation decreases. We show in Figure 4 the results of our Monte Carlo simulation for a range of N values. These simulations make the simplifying assumption that the light curve follows a basic sinusoidal profile as would be expected for a rotating extended triaxial ellipsoid. More realistic light curve shapes with asymmetries could potentially alter the results if these deviations changed the fraction of the light curve that was near the extrema. However, the unknown light curve amplitude is a much more dominant source of uncertainty in this analysis than the non-sinusoidal shape or the range of amplitude deviations seen in Figure 4.

In order to translate this deviation from a percentage of amplitude A to a measured magnitude deviation, we use the observed light curve amplitudes of all NEOs automatically detected by NEOWISE during the first three years of the Reactivation survey (Nugent et al. 2015, 2016; Masiero et al. 2017). The mean observed $W2$ magnitude variation (an analog for light curve amplitude) is 0.57 mag, and the median is 0.5 mag. These numbers are the same if we consider only the 32 NEOs smaller than $D < 250$ m. Therefore a single observation has a typical uncertainty of 32% $A = 0.32 \times 0.57$ mag ~0.2 mag from the light curve mean, which corresponds to ~20% in flux or ~10% in diameter. Using the maximum observed magnitude variation of $A \sim 1.8$ mag would result in an uncertainty of ~60% in flux or ~30% in diameter. Conversely, an object observed pole-on, or that is spherical, would present no apparent light curve variations and thus no additional uncertainty from the small number of observations. However, without more data on the spin state of each object, we cannot place a better constraint on this uncertainty and thus default to the mean value.

This uncertainty decreases with the square-root of the number of observations as shown by the average of all simulations in Figure 4. As noted in Mainzer et al. (2014b), the true value of this error for an individual object is highly dependent on the actual light curve amplitude, triaxial shape, and viewing geometry. Additionally, this error is not distributed normally around the best-fit diameter, as an object is more likely to be seen at the brightest excursion from its true mean flux as noted by the analysis from the *Infrared Astronomical Satellite* mission.[11] Thus, the diameters presented here will preferentially over-estimate the true size

[11] https://irsa.ipac.caltech.edu/IRASdocs/exp.sup/ch11/J.html

Table 1
Thermal Model Fits for Short arc NEOs Observed in the First Three Years of the NEOWISE Reactivation Survey

Name	H (mag)	G	Diameter (km)	$D_{\rm corr}$ (km)	$\log p_V$	$\log p_{V_{\rm corr}}$	Beaming	n_{W1}	n_{W2}	Phase (deg)	Fitted Beaming?
K14A00C	21.00	0.15	0.343 ± 0.094	0.316	−1.22 ± 0.31	−1.15	2.00 ± 1.00	0	1	71.37	0
K14A16G	22.70	0.15	0.200 ± 0.032	0.165	−1.43 ± 0.13	−1.28	1.76 ± 0.23	4	4	86.35	1
K14A51N	20.50	0.15	0.222 ± 0.073	0.193	−0.65 ± 0.24	−0.53	2.00 ± 1.00	0	1	80.29	0
K14B02X	21.90	0.15	0.110 ± 0.030	0.097	−0.60 ± 0.21	−0.49	0.67 ± 0.20	2	2	78.46	1
K14B08R	21.70	0.15	0.141 ± 0.040	0.118	−0.73 ± 0.24	−0.59	2.00 ± 1.00	0	3	84.57	0
K14B25H	21.60	0.15	0.257 ± 0.033	0.219	−1.21 ± 0.09	−1.08	1.25 ± 0.13	3	3	82.58	1
K14C00R	22.50	0.15	0.116 ± 0.014	0.094	−1.03 ± 0.12	−0.86	2.95 ± 0.15	1	1	88.02	1
K14C13D	21.30	0.15	0.398 ± 0.055	0.338	−1.47 ± 0.13	−1.34	1.30 ± 0.10	1	1	82.85	1
K14F00D	25.50	0.15	0.022 ± 0.005	0.018	−0.65 ± 0.20	−0.48	2.00 ± 1.00	0	1	89.08	0
K14G35J	20.30	0.15	0.377 ± 0.115	0.351	−1.03 ± 0.34	−0.96	2.00 ± 1.00	0	2	69.88	0
K14H04G	19.80	0.15	0.975 ± 0.099	0.883	−1.65 ± 0.09	−1.56	1.76 ± 0.13	4	4	74.56	1
K14J55V	20.10	0.15	0.321 ± 0.100	0.290	−0.81 ± 0.27	−0.72	2.00 ± 1.00	0	2	74.82	0
K14K76O	23.90	0.15	0.166 ± 0.043	0.141	−1.75 ± 0.27	−1.62	2.00 ± 1.00	0	4	82.73	0
K14K86V	20.30	0.15	0.644 ± 0.173	0.618	−1.49 ± 0.20	−1.45	2.00 ± 1.00	0	2	63.68	0
K14M05S	22.70	0.15	0.113 ± 0.030	0.093	−0.94 ± 0.23	−0.79	2.00 ± 1.00	0	1	85.82	0
K14M18F	26.00	0.15	0.069 ± 0.020	0.057	−1.83 ± 0.22	−1.68	2.00 ± 1.00	0	5	85.18	0
K14N03E	20.10	0.15	0.233 ± 0.051	0.202	−0.53 ± 0.20	−0.41	2.00 ± 1.00	0	2	80.82	0
K14N52K	21.30	0.15	0.502 ± 0.170	0.462	−1.67 ± 0.38	−1.60	2.00 ± 1.00	0	4	71.77	0
K14P59S	20.50	0.15	0.206 ± 0.051	0.181	−0.58 ± 0.19	−0.47	2.00 ± 1.00	0	5	78.84	0
K14P59W	20.90	0.15	0.412 ± 0.048	0.352	−1.34 ± 0.09	−1.21	1.41 ± 0.10	2	2	82.49	1
K14QT5T	25.90	0.15	0.041 ± 0.011	0.033	−1.34 ± 0.36	−1.18	2.00 ± 1.00	0	2	87.56	0
K14SE1V	21.60	0.15	0.172 ± 0.043	0.149	−0.86 ± 0.26	−0.75	2.00 ± 1.00	0	8	80.37	0
K14SQ0U	21.80	0.15	0.174 ± 0.049	0.149	−0.95 ± 0.28	−0.83	2.00 ± 1.00	0	2	81.36	0
K14V02G	22.70	0.15	0.085 ± 0.025	0.073	−0.70 ± 0.33	−0.57	2.00 ± 1.00	0	5	82.87	0
K14V02K	18.70	0.15	0.691 ± 0.161	0.648	−0.91 ± 0.20	−0.85	2.00 ± 1.00	0	6	68.40	0
K14V06L	21.30	0.15	0.242 ± 0.081	0.211	−1.04 ± 0.25	−0.93	1.54 ± 0.43	3	3	80.16	1
K14W06L	20.00	0.15	0.198 ± 0.043	0.176	−0.28 ± 0.16	−0.18	1.24 ± 0.29	3	2	77.51	1
K14WC0Z	20.50	0.15	0.297 ± 0.078	0.245	−0.90 ± 0.24	−0.75	2.06 ± 0.47	2	2	85.93	1
K14Wa8K	21.40	0.15	0.486 ± 0.103	0.441	−1.69 ± 0.27	−1.60	2.00 ± 1.00	0	3	74.14	0
K14Y14L	20.60	0.15	0.355 ± 0.067	0.304	−1.09 ± 0.15	−0.97	1.68 ± 0.24	1	1	81.78	1
K15BV0W	22.00	0.15	0.146 ± 0.015	0.126	−0.88 ± 0.08	−0.76	0.89 ± 0.08	4	4	81.16	1
K15Bo9N	20.70	0.15	0.315 ± 0.067	0.274	−1.03 ± 0.17	−0.91	2.00 ± 1.00	0	4	80.17	0
K15C12X	20.00	0.15	0.184 ± 0.051	0.154	−0.27 ± 0.20	−0.13	0.85 ± 0.25	1	1	84.54	1
K15C13P	19.80	0.15	0.384 ± 0.098	0.334	−0.84 ± 0.19	−0.73	1.54 ± 0.34	4	4	80.25	1
K15D54A	20.80	0.15	0.468 ± 0.058	0.392	−1.41 ± 0.12	−1.27	1.18 ± 0.07	1	1	84.57	1
K15DI0U	20.80	0.15	0.435 ± 0.179	0.397	−1.35 ± 0.45	−1.27	2.00 ± 1.00	0	1	73.33	0
K15DL5N	19.80	0.15	0.535 ± 0.109	0.453	−1.13 ± 0.15	−1.00	1.88 ± 0.30	2	2	83.46	1
K15E07D	20.80	0.15	0.313 ± 0.068	0.278	−1.06 ± 0.24	−0.96	2.00 ± 1.00	0	1	77.15	0
K15E07E	20.20	0.15	0.294 ± 0.074	0.262	−0.77 ± 0.19	−0.67	2.00 ± 1.00	0	6	77.05	0
K15F00L	20.80	0.15	0.232 ± 0.040	0.197	−0.88 ± 0.23	−0.75	2.75 ± 0.38	2	2	82.70	1
K15F33S	22.20	0.15	0.066 ± 0.014	0.054	−0.27 ± 0.16	−0.11	0.90 ± 0.24	1	2	87.52	1
K15FC0N	23.50	0.15	0.064 ± 0.019	0.056	−0.76 ± 0.21	−0.65	0.96 ± 0.27	1	1	80.06	1
K15G00S	20.60	0.15	0.262 ± 0.063	0.232	−0.83 ± 0.29	−0.73	2.00 ± 1.00	0	2	77.53	0
K15H01F	22.70	0.15	0.108 ± 0.023	0.095	−0.90 ± 0.19	−0.79	2.00 ± 1.00	0	3	78.78	0
K15HH1U	23.70	0.15	0.108 ± 0.033	0.089	−1.30 ± 0.43	−1.14	2.00 ± 1.00	0	4	86.91	0
K15HI1X	23.90	0.15	0.078 ± 0.021	0.064	−1.10 ± 0.21	−0.94	2.00 ± 1.00	0	1	87.52	0
K15J02C	21.00	0.15	0.382 ± 0.099	0.350	−1.32 ± 0.26	−1.24	2.00 ± 1.00	0	4	72.71	0
K15KC2N	20.50	0.15	0.342 ± 0.086	0.311	−1.02 ± 0.26	−0.94	2.00 ± 1.00	0	4	73.84	0
K15L21L	19.90	0.15	0.374 ± 0.074	0.331	−0.86 ± 0.20	−0.76	1.19 ± 0.23	3	3	77.91	1
K15L21M	22.10	0.15	0.066 ± 0.013	0.056	−0.23 ± 0.14	−0.10	0.71 ± 0.15	1	1	82.20	1
K15MB6N	19.80	0.15	0.394 ± 0.095	0.365	−0.86 ± 0.25	−0.79	2.00 ± 1.00	0	8	71.06	0
K15N13Z	20.60	0.15	0.258 ± 0.075	0.219	−0.82 ± 0.21	−0.68	1.48 ± 0.38	1	1	83.06	1
K15P00C	19.40	0.15	1.266 ± 0.230	1.159	−1.72 ± 0.15	−1.64	2.21 ± 0.30	4	4	72.89	1
K15P57K	24.70	0.15	0.075 ± 0.020	0.062	−1.38 ± 0.36	−1.23	2.00 ± 1.00	0	3	86.34	0
K15PM8U	20.30	0.15	0.328 ± 0.106	0.282	−0.90 ± 0.33	−0.78	2.00 ± 1.00	0	1	81.58	0
K15Q00G	23.80	0.15	0.132 ± 0.045	0.109	−1.51 ± 0.57	−1.36	2.00 ± 1.00	0	1	85.55	0
K15T00E	22.50	0.15	0.156 ± 0.035	0.128	−1.14 ± 0.21	−0.98	1.46 ± 0.26	1	1	86.66	1
K15T24X	21.50	0.15	0.252 ± 0.046	0.208	−1.16 ± 0.14	−1.00	1.27 ± 0.19	3	3	86.05	1
K15TN8K	21.90	0.15	0.076 ± 0.029	0.067	−0.27 ± 0.27	−0.16	0.90 ± 0.35	1	1	78.54	1
K15TW3D	19.90	0.15	0.332 ± 0.072	0.307	−0.76 ± 0.19	−0.68	2.00 ± 1.00	0	2	71.40	0
K15U67M	18.90	0.15	0.665 ± 0.183	0.577	−0.96 ± 0.30	−0.84	2.35 ± 0.57	2	2	80.36	1
K15V01E	21.00	0.15	0.139 ± 0.067	0.112	−0.43 ± 0.34	−0.26	1.35 ± 0.65	3	3	88.50	1
K15V01F	23.80	0.15	0.072 ± 0.021	0.059	−0.99 ± 0.31	−0.83	2.00 ± 1.00	0	2	86.48	0

Table 1
(Continued)

Name	H (mag)	G	Diameter (km)	$D_{\rm corr}$ (km)	$\log p_V$	$\log p_{V_{\rm corr}}$	Beaming	n_{W1}	n_{W2}	Phase (deg)	Fitted Beaming?
K15V65B	22.90	0.15	0.049 ± 0.026	0.042	−0.29 ± 0.37	−0.16	0.91 ± 0.53	2	2	82.11	1
K15V65U	26.40	0.15	0.047 ± 0.015	0.037	−1.65 ± 0.33	−1.48	2.00 ± 1.00	0	1	89.35	0
K15W09G	20.30	0.15	0.480 ± 0.062	0.412	−1.32 ± 0.14	−1.20	3.14 ± 0.23	1	1	81.88	1
K15W13H	19.00	0.15	1.403 ± 0.129	1.305	−1.65 ± 0.08	−1.58	1.65 ± 0.10	3	3	70.20	1
K15X00E	24.70	0.15	0.048 ± 0.012	0.042	−1.00 ± 0.32	−0.89	2.00 ± 1.00	0	4	79.37	0
K15X01D	20.10	0.15	0.201 ± 0.082	0.177	−0.40 ± 0.29	−0.29	0.95 ± 0.41	3	3	78.42	1
K15X01K	20.00	0.15	0.350 ± 0.092	0.325	−0.84 ± 0.24	−0.77	2.00 ± 1.00	0	6	70.50	0
K15XC9O	25.20	0.15	0.060 ± 0.015	0.053	−1.39 ± 0.24	−1.29	2.00 ± 1.00	0	2	78.85	0
K15Y00K	25.90	0.15	0.046 ± 0.014	0.038	−1.43 ± 0.38	−1.28	2.00 ± 1.00	0	5	86.51	0
K15Y01B	21.50	0.15	0.186 ± 0.047	0.161	−0.89 ± 0.20	−0.77	2.00 ± 1.00	0	2	80.73	0
K15Y07X	22.00	0.15	0.110 ± 0.017	0.095	−0.64 ± 0.12	−0.52	1.09 ± 0.17	6	7	81.46	1
K15Y10T	20.00	0.15	0.359 ± 0.099	0.339	−0.86 ± 0.32	−0.81	2.00 ± 1.00	0	7	67.38	0
K16AG6D	23.60	0.15	0.077 ± 0.021	0.063	−0.96 ± 0.19	−0.80	2.00 ± 1.00	0	1	87.23	0
K16B14P	21.20	0.15	0.285 ± 0.073	0.264	−1.14 ± 0.24	−1.07	2.00 ± 1.00	0	5	70.57	0
K16B15J	23.30	0.15	0.080 ± 0.013	0.064	−0.95 ± 0.24	−0.77	2.76 ± 0.41	2	2	89.01	1
K16B80R	21.30	0.15	0.208 ± 0.056	0.181	−0.91 ± 0.27	−0.80	2.00 ± 1.00	0	4	79.97	0
K16C30U	21.60	0.15	0.459 ± 0.111	0.435	−1.72 ± 0.27	−1.66	2.00 ± 1.00	0	5	66.42	0
K16C31B	25.00	0.15	0.070 ± 0.020	0.056	−1.44 ± 0.26	−1.26	2.00 ± 1.00	0	2	89.10	0
K16CD6A	19.30	0.15	0.654 ± 0.193	0.649	−1.10 ± 0.37	−1.09	2.00 ± 1.00	0	13	52.31	0
K16CD6L	21.40	0.15	0.123 ± 0.057	0.113	−0.50 ± 0.33	−0.42	1.50 ± 0.67	3	3	72.90	1
K16D02O	23.70	0.15	0.034 ± 0.009	0.031	−0.27 ± 0.19	−0.18	0.93 ± 0.30	2	2	75.26	1
K16E01E	24.50	0.15	0.066 ± 0.022	0.055	−1.19 ± 0.24	−1.05	2.10 ± 0.54	1	1	84.89	1
K16E01V	23.90	0.15	0.106 ± 0.023	0.095	−1.36 ± 0.22	−1.27	2.00 ± 1.00	0	2	76.55	0
K16E26Z	22.60	0.15	0.268 ± 0.080	0.227	−1.65 ± 0.31	−1.51	2.00 ± 1.00	0	6	83.45	0
K16EF7H	21.10	0.15	0.231 ± 0.054	0.213	−0.92 ± 0.20	−0.84	2.00 ± 1.00	0	5	71.61	0
K16F03Y	21.30	0.15	0.205 ± 0.055	0.163	−0.90 ± 0.37	−0.72	2.49 ± 0.59	1	1	90.16	1
K16F12E	20.60	0.15	0.202 ± 0.042	0.171	−0.61 ± 0.21	−0.47	2.00 ± 1.00	0	3	83.84	0
K16F13C	22.00	0.15	0.186 ± 0.060	0.163	−1.09 ± 0.27	−0.98	2.00 ± 1.00	0	4	78.72	0
K16GM0P	21.90	0.15	0.422 ± 0.128	0.406	−1.76 ± 0.33	−1.72	2.00 ± 1.00	0	2	63.10	0
K16J17M	19.60	0.15	0.661 ± 0.205	0.648	−1.23 ± 0.25	−1.21	2.00 ± 1.00	0	3	57.25	0
K16J28W	25.40	0.15	0.031 ± 0.010	0.029	−0.91 ± 0.35	−0.83	2.00 ± 1.00	0	1	73.71	0
K16J33U	20.70	0.15	0.174 ± 0.092	0.156	−0.52 ± 0.36	−0.42	1.32 ± 0.65	2	2	75.98	1
K16K00D	22.30	0.15	0.160 ± 0.046	0.144	−1.08 ± 0.44	−0.99	2.00 ± 1.00	0	4	75.78	0
K16L00B	22.80	0.15	0.060 ± 0.017	0.048	−0.28 ± 0.21	−0.11	1.28 ± 0.40	4	4	87.95	1
K16L02F	22.40	0.15	0.204 ± 0.050	0.189	−1.33 ± 0.19	−1.26	2.00 ± 1.00	0	9	71.09	0
K16L09D	22.40	0.15	0.085 ± 0.022	0.078	−0.57 ± 0.19	−0.49	0.92 ± 0.22	1	1	73.03	1
K16L47V	20.00	0.15	0.237 ± 0.115	0.205	−0.50 ± 0.34	−0.38	1.12 ± 0.51	3	3	81.05	1
K16P00N	20.40	0.15	0.160 ± 0.068	0.135	−0.31 ± 0.30	−0.17	1.30 ± 0.57	2	2	83.46	1
K16P00T	20.60	0.15	0.647 ± 0.050	0.626	−1.61 ± 0.09	−1.58	1.09 ± 0.06	7	7	61.80	1
K16P08O	20.00	0.15	0.479 ± 0.172	0.438	−1.11 ± 0.55	−1.03	2.00 ± 1.00	0	10	72.99	0
K16R00W	23.20	0.15	0.066 ± 0.020	0.054	−0.67 ± 0.22	−0.51	0.88 ± 0.25	1	1	86.70	1
K16R40M	24.70	0.15	0.081 ± 0.012	0.071	−1.49 ± 0.14	−1.38	2.93 ± 0.26	1	1	79.68	1
K16S02G	20.60	0.15	0.278 ± 0.092	0.240	−0.88 ± 0.29	−0.76	2.00 ± 1.00	0	1	81.21	0
K16T11B	25.20	0.15	0.018 ± 0.006	0.014	−0.34 ± 0.25	−0.17	0.58 ± 0.26	1	1	88.54	1
K16T17X	23.50	0.15	0.063 ± 0.017	0.051	−0.75 ± 0.23	−0.58	2.00 ± 1.00	0	1	88.14	0
K16T19Z	23.10	0.15	0.050 ± 0.008	0.045	−0.31 ± 0.10	−0.22	1.14 ± 0.18	1	1	74.53	1
K16T56M	26.80	0.15	0.008 ± 0.002	0.007	−0.33 ± 0.21	−0.18	0.54 ± 0.18	1	1	85.61	1
K16T57A	20.80	0.15	0.281 ± 0.047	0.254	−1.06 ± 0.21	−0.97	2.80 ± 0.37	2	2	74.75	1
K16U25Z	21.60	0.15	0.143 ± 0.054	0.131	−0.71 ± 0.27	−0.63	1.31 ± 0.45	1	1	72.80	1
K16U41D	22.80	0.15	0.049 ± 0.012	0.044	−0.25 ± 0.18	−0.16	0.85 ± 0.23	2	3	74.32	1
K16UA1H	22.70	0.15	0.067 ± 0.028	0.060	−0.48 ± 0.31	−0.39	1.21 ± 0.51	2	2	74.69	1
K16W48N	24.80	0.15	0.144 ± 0.039	0.129	−1.99 ± 0.21	−1.89	2.00 ± 1.00	0	2	76.78	0
K16X18A	23.10	0.15	0.065 ± 0.015	0.059	−0.62 ± 0.19	−0.53	2.00 ± 1.00	0	1	76.04	0

Note. Names are in MPC-packed format, H and G are the photometric parameters, p_V is the visible-light albedo, n_{W1} and n_{W2} are the numbers of detections in the $W1$ and $W2$ bandpasses, the fitted beaming column is "1" if the beaming parameter was fitted during the NEATM modeling and "0" if an assumed value was used. $D_{\rm corr}$ and $pV_{\rm corr}$ are the phase-corrected diameter using the equations from Mommert et al. (2018).

of these NEOs. We include the typical additional uncertainty in quadrature with the diameter error calculated from the Monte Carlo trials, but note that there could be a much larger additional diameter error of order 30% for specific cases. We estimate this component of the error ($\sigma_{\rm LC}$) based on the number of observations in $W2$ ($n_{\rm obs}$), using the equation:

$$\sigma_{\rm LC} = \frac{0.10D}{\sqrt{n_{\rm obs}}}$$

and we propagate this error to the error on albedo as well.

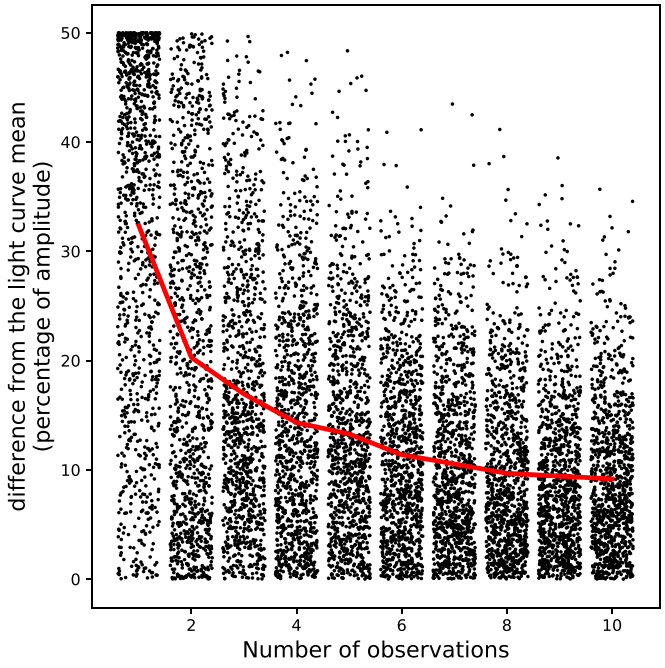

Figure 4. Outcome of a Monte Carlo simulation of N randomly spaced observations of a theoretical asteroid light curve, showing the resulting deviation between the measured mean value and the actual light curve mean as a percentage of amplitude A. Each point is given an offset in the range of $(-0.4, 0.4)$ from the integer N observations for clarity. The average of all trials (red line) decreases as the square-root of number of observations of the light curve.

Recently, Mommert et al. (2018) have shown that the NEATM model does not perform as well at phase angles larger than $\alpha > 65°$ as it does for smaller phase angles, and frequently overestimates the diameter of NEOs seen at these phases. This will be an additional source of uncertainty on top of the incomplete light curve sampling. As nearly all of the objects presented in this paper are at large phase angles, we apply the high-phase NEATM diameter and albedo correction terms from Mommert et al. (2018) to our fits, and present these as separate columns in Table 1.

4. Results and Discussion

Of the 122 objects that were detected, 5 thermal fits were rejected due to a reflected light contribution of >10% in the *W*2 band. One object, 2016 TB57, was not fit because it has only two detections, both of which had magnitude errors larger than the threshold of 0.25 mag, and thus insufficient for constraining the thermal emission.

Thermal infrared fits for 116 small NEOs are presented in Table 1. We compare the diameters and albedos found here with those of all NEOs measured that were detected by WMOPS during the reactivated NEOWISE mission (Nugent et al. 2015, 2016; Masiero et al. 2017) in Figure 5. The short-arc objects we report here tend to be significantly smaller than the objects detected by WMOPS, as would be expected for objects passing close to the Earth and thus moving quickly across the field of view. Additionally, we see imprinted in the population a bias against small, low albedo NEOs. This is an artifact of the flux-limited Malmquist bias that impacts the ground-based visible-light surveys that discovered the short-arc objects. In contrast, the NEOWISE-detected objects show a

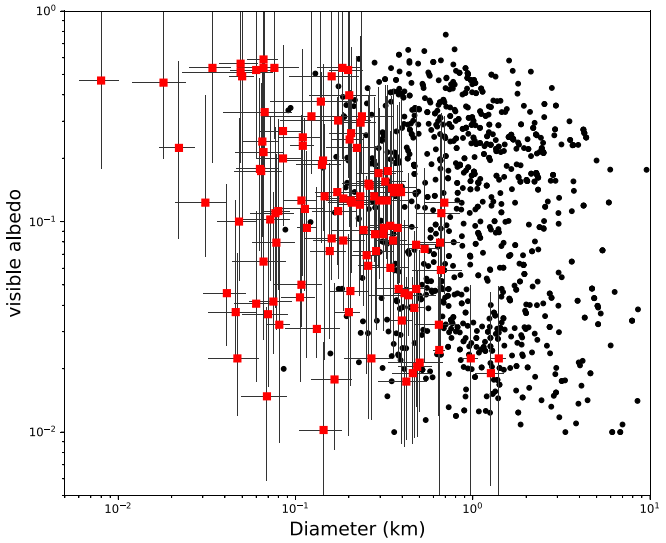

Figure 5. Comparison of fitted diameters and albedos for the short-arc objects presented here (red squares) with the NEOs found by the automated detection routines during the first three years of the reactivated NEOWISE survey (black). The short-arc objects tend to be smaller than objects detected automatically, and show a significant bias against small, low albedo asteroids that is a result of the visible-light selection effects imposed by the ground-based surveys that discovered this population. Error bars on previously reported objects are omitted for clarity.

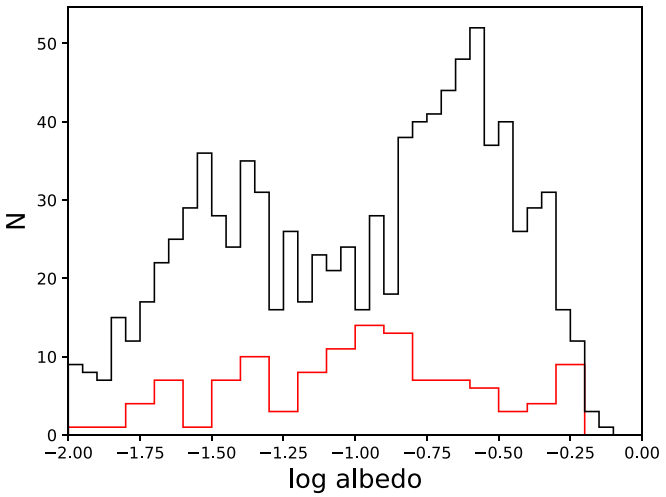

Figure 6. Histogram of the albedos of the short-arc objects reported here (red) and previously reported NEOs characterized by NEOWISE (black). Note the bins for newly reported objects are twice as wide as those for previously reported NEOs.

nearly uniform sensitivity with respect to albedo, as observed for previous phases of the *WISE* survey (Mainzer et al. 2011b).

Looking at the albedos alone, we show in Figure 6 the distributions of albedos for both the short-arc population reported here and the population of objects previously reported. While the histogram of previously reported objects shows the expected bimodal albedo distribution (Mainzer et al. 2011b), the short-arc objects are skewed toward higher albedos when compared with the population selected based on *W*2 flux. Although the distribution of albedos in this work have relatively few objects in each bin, a KS test allows us to reject the assumption that they are drawn from the same population at the >98% level. The difference albedo distributions is likely an artifact of the incomplete rotation phase coverage coupled with

the Eddington bias favoring detection at an object's brighter apparition. For these cases, the NEOWISE diameter fit will be systematically greater than the true effective spherical diameter, which will result in a shift in fitted albedo to lower values (for a fixed absolute magnitude). Thus, the population of objects with $p_V \sim 10\%$ likely will have over-estimated diameters and under-estimated albedos, which would shift them to the bright peak in the albedo histogram. This shift would be in addition to the phase-correction to NEATM. However, as we cannot know which specific objects are suffering from this bias without other data, we cannot correct for it. Instead, we encourage caution in interpretation of these results, especially when comparing to results drawn from the WMOPS-detected sample, which is selected based on the thermal emission-dominated *W*2 flux as opposed to reflected visible-light flux.

5. Conclusions

We present diameter fits for 116 short-arc NEOs seen during the first three years of the reactivated NEOWISE survey. Combined with the 541 unique NEOs that were automatically detected and characterized over that time, NEOWISE has provided characterization data for 657 NEOs since the survey was restarted in 2013. This brings the total count of NEOs with thermal infrared characterization from all phases of the *WISE* and NEOWISE surveys to 1203, which represents 7% of the known NEO population at the time of writing. The analysis presented here shows the utility of recording and archiving full-frame images from surveys, as it allows later searches for objects that were missed during automatic processing, greatly enhancing the scientific return of these data.

We thank the referee for their detailed and helpful comments that improved the manuscript. This research was carried out at the Jet Propulsion Laboratory, California Institute of Technology, under a contract with the National Aeronautics and Space Administration. This publication makes use of data products from the *Wide-field Infrared Survey Explorer*, which is a joint project of the University of California, Los Angeles, and the Jet Propulsion Laboratory/California Institute of Technology, funded by the National Aeronautics and Space Administration. This publication also makes use of data products from NEOWISE, which is a project of the Jet Propulsion Laboratory/California Institute of Technology, funded by the Planetary Science Division of the National Aeronautics and Space Administration. This research has made use of data and services provided by the International Astronomical Union's Minor Planet Center. This research has made use of the NASA/IPAC Infrared Science Archive, which is operated by the California Institute of Technology, under contract with the National Aeronautics and Space Administration.

ORCID iDs

Joseph R. Masiero https://orcid.org/0000-0003-2638-720X
R. M. Cutri https://orcid.org/0000-0002-0077-2305
T. Grav https://orcid.org/0000-0002-3379-0534
E. L. Wright https://orcid.org/0000-0001-5058-1593

References

Bowell, E., Hapke, B., Domingue, D., et al. 1989, Asteroids II (Tucson, AZ: Univ. Arizona Press), 524
Cutri, R. M., Mainzer, A., Conrow, T., et al. 2015, Explanatory Supplement to the NEOWISE Data Release Products, http://wise2.ipac.caltech.edu/docs/release/neowise/expsup/
Cutri, R. M., Wright, E. L., Conrow, T., et al. 2014, Explanatory Supplement to the AllWISE Data Release Products, http://wise2.ipac.caltech.edu/docs/release/allwise/expsup/
Harris, A. W. 1998, Icar, 131, 291
Jones, E., Oliphant, E., Peterson, P., et al. 2001, SciPy: Open Source Scientific Tools for Python, https://www.scipy.org/
Lagerkvist, C.-I., & Magnusson, P. 1990, A&AS, 86, 119
Mainzer, A. K., Bauer, J., Cutri, R., et al. 2014a, ApJ, 792, 30
Mainzer, A. K., Bauer, J., Grav, T., et al. 2014b, ApJ, 784, 110
Mainzer, A. K., Bauer, J. M., Grav, T., et al. 2011a, ApJ, 731, 53
Mainzer, A. K., Grav, T., Bauer, J. M., et al. 2011b, ApJ, 743, 156
Masiero, J. R., Nugent, C., Mainzer, A. K., et al. 2017, AJ, 154, 168
Mommert, M., Hora, J. L., Harris, A. W., et al. 2014, ApJ, 781, 25
Mommert, M., Jedicke, R., & Trilling, D. 2018, AJ, 155, 74
Myhrvold, N. 2018, Icar, 303, 91
Nugent, C. R., Mainzer, A., Bauer, J. M., et al. 2016, AJ, 152, 63
Nugent, C. R., Mainzer, A., Masiero, J., et al. 2015, ApJ, 814, 117
Tholen, D. J. 2009, Asteroid Absolute Magnitudes V12.0. EAR-A-5-DDR-ASTERMAG-V12.0. NASA Planetary Data System, https://sbn.psi.edu/pds/resource/astermag.html
Vereš, P., Jedicke, R., Fitzsimmons, A., et al. 2015, Icar, 261, 34
Wolters, S., & Green, S. 2009, MNRAS, 400, 204